Femtosecond tracking of carrier relaxation in germanium with extreme ultraviolet transient reflectivity

Christopher J. Kaplan,[1] Peter M. Kraus,[1] Andrew D. Ross,[1] Michael Zürch,[1] Scott K. Cushing,[1] Marieke F. Jager,[1] Hung-Tzu Chang,[1] Eric M. Gullikson,[2] Daniel M. Neumark,[1,3] and Stephen R. Leone[1,3,4]

[1]*Department of Chemistry, University of California, Berkeley, California 94720, USA*

[2]*Center for X-ray Optics, Lawrence Berkeley National Laboratory, Berkeley, California 94720, USA*

[3]*Chemical Sciences Division, Lawrence Berkeley National Laboratory, USA*

[4]*Department of Physics, University of California, Berkeley, California 94720, USA*

(Received 21 February 2018; published 8 May 2018)

Extreme ultraviolet (XUV) transient reflectivity around the germanium $M_{4,5}$ edge ($3d$ core-level to valence transition) at 30 eV is advanced to obtain the transient dielectric function of crystalline germanium [100] on femtosecond to picosecond time scales following photoexcitation by broadband visible-to-infrared (VIS/NIR) pulses. By fitting the transient dielectric function, carrier-phonon induced relaxations are extracted for the excited carrier distribution. The measurements reveal a hot electron relaxation rate of 3.2 ± 0.2 ps attributed to the X-L intervalley scattering and a hot hole relaxation rate of 600 ± 300 fs ascribed to intravalley scattering within the heavy hole (HH) band, both in good agreement with previous work. An overall energy shift of the XUV dielectric function is assigned to a thermally induced band gap shrinkage by formation of acoustic phonons, which is observed to be on a timescale of 4–5 ps, in agreement with previously measured optical phonon lifetimes. The results reveal that the transient reflectivity signal at an angle of 66° with respect to the surface normal is dominated by changes to the real part of the dielectric function, due to the near critical angle of incidence of the experiment (66°–70°) for the range of XUV energies used. This work provides a methodology for interpreting XUV transient reflectivity near core-level transitions, and it demonstrates the power of the XUV spectral region for measuring ultrafast excitation dynamics in solids.

DOI: 10.1103/PhysRevB.97.205202

I. INTRODUCTION

Understanding the electronic response of solids to ultrashort laser pulses is crucial for developing efficient optoelectronics [1], hot carrier solar utilization [2], and other semiconductor based devices. Recently, extreme ultraviolet (XUV) transient absorption was shown to be capable of simultaneously recording separate electron and hole dynamics in nanocrystalline germanium thin films in a single measurement [3,4]. This work confirmed intervalley scattering rates and revealed the timescales of carrier-recombination at defect-rich grain boundaries of nanocrystals through a Shockley-Read-Hall mechanism. These results highlight the ability of XUV transient absorption to provide a spectrally resolved probe of complex dynamics in solids [5–7]. However, electron and hole relaxation kinetics measured in these films were ultimately limited by the high defect density in the thin film samples, and the results were not characteristic of the intrinsic, high purity, material itself. This discrepancy highlights drawbacks of XUV transient absorption in solids, namely that it can only be applied to very thin films (<100 nm). These thin films are difficult to obtain and can be of questionable relevance to representative semiconductors, due to their low thermal conductivity and defect rich structure. Developing a tool to provide a spectrally resolved, sub-femtosecond probe of carrier dynamics in well-defined, single-crystal samples remains a significant challenge in unraveling ultrafast processes in solids.

In contrast to absorption, XUV reflectivity allows spectroscopic access to dynamics in optically thick, well-defined samples, greatly extending the set of systems in which XUV spectroscopy can be applied [8–12]. Static XUV reflection spectra from high harmonic sources have been demonstrated and shown to provide excellent surface sensitivity [13,14]. Quite recently, XUV transient reflectivity (XUV TR) was used for time-resolved spectroscopic observation of surface electron dynamics in metal oxides [15]. This work highlighted the sensitivity of reflectivity to the full dielectric function $\varepsilon(\omega) = \varepsilon_1(\omega) + i\varepsilon_2(\omega)$, including both the dispersive part $\varepsilon_1(\omega)$, and the absorptive part $i\varepsilon_2(\omega)$.

Despite these advances, questions such as the relative sensitivity of XUV TR to electronic or lattice dynamics, and the role of the real vs imaginary parts of the dielectric function have yet to be explored. These questions are made more difficult by the fact that few XUV TR experiments to date have been performed on single crystal samples. Accordingly, comparison of XUV TR to the wide body of optical transient reflectivity in single-crystal semiconductors is difficult.

To surmount these challenges, here we develop XUV transient reflectivity to measure the time-resolved XUV dielectric function of single-crystal germanium, a widely employed group-IV semiconductor. By monitoring reflectivity around the Ge $M_{4,5}$ absorption edge subsequent to excitation with a few-cycle 800 nm pump pulse, the XUV core-level transitions provide a spectrally resolved, ultrafast probe of carrier dynamics in the valence and conduction bands. The time-resolved XUV dielectric function is retrieved from the data, allowing spectral separation of electrons, holes, and band shift contributions to the observed transient reflectivity. Analysis

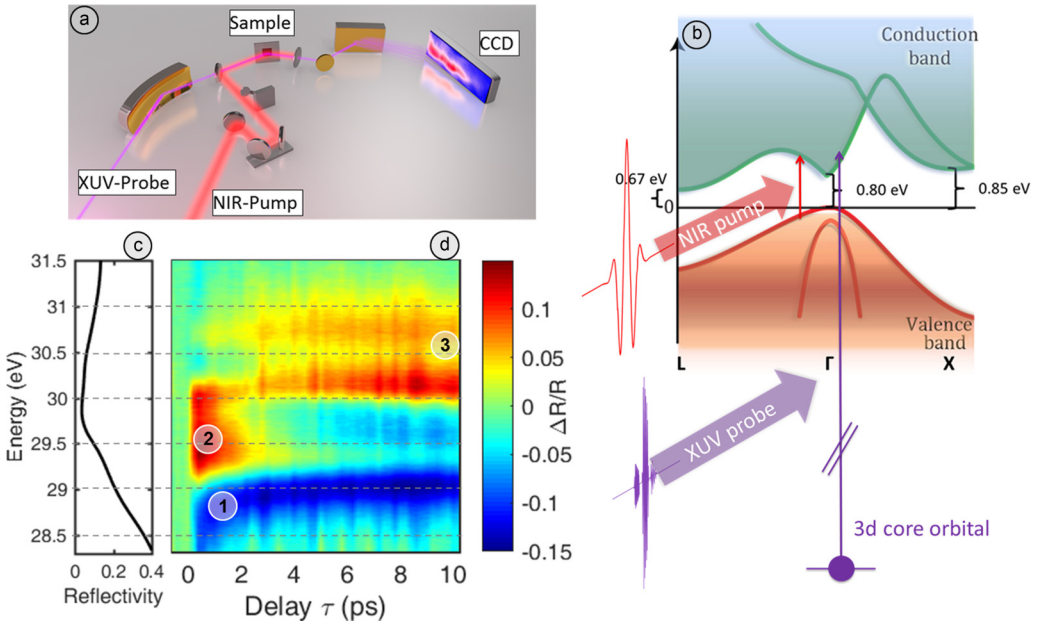

FIG. 1. Femtosecond transient reflectivity in germanium. (a) A time delayed XUV pulse probe transient reflectivity in single-crystal germanium, after excitation with a few cycle NIR pump pulse. (b). The NIR pump promotes electrons from the valence band (red) to the conduction band (green). Subsequently, reflectivity of the XUV probes the excited carrier distribution via transitions from 3*d* core states to the valence and conduction bands at the $M_{4,5}$ edge. (c) Static reflectivity of germanium at 66° angle of incidence, *s* polarization. (d). Raw transient reflectivity data measured, with marked reflectivity features 1, 2, and 3 as described in text.

of the recovered transient dielectric function reveals that the XUV TR signal contains information from both the real and imaginary parts of the dielectric function and that the real part is more significant at the reflection angle chosen. Further, kinetic analysis of the retrieved dielectric function allows extraction of electron, hole, and lattice relaxation timescales. The measurements reveal a hot electron relaxation rate of 3.2 ± 0.2 ps attributed to the X-L intervalley scattering and a hot hole relaxation rate of 600 ± 300 fs ascribed to intravalley scattering within the heavy hole (HH) band, both in good agreement with previous work. An overall energy shift of the XUV dielectric function is assigned to band gap renormalization due to the formation of acoustic phonons, which is observed to be on a timescale of 4 ± 1 ps, in agreement with previously measured optical phonon lifetimes.

II. EXPERIMENTAL SETUP

The apparatus [Fig. 1(a)] consists of an 800 nm Ti/sapphire laser, which is used to generate high harmonics (HHG) [16], a toroidal focusing mirror, a Ge(100) sample, a variable time delay line, a variable line spaced grating, and an x-ray CCD camera to detect the reflected signal from the sample.

In the experiment, a NIR (near infrared) 5-fs pulse, spanning a bandwidth from 550–1000 nm, is focused collinearly with a time-delayed subfemtosecond XUV pulse created by high harmonic generation (HHG) [16] onto a single-crystal germanium [100] wafer [Fig. 1(a)] at an angle of 66° from the normal. This angle was constrained by the geometric configuration of the apparatus, but the value is fortuitous because it is near the critical angle in the XUV wavelength range of interest, which will be discussed further below. While the apparatus has the capability to measure subfemtosecond processes, the results here focus on the many-femtosecond to picosecond timescales to perform an analysis of the transient reflectivity dielectric function and carrier-phonon processes in germanium. The NIR pulse photoexcites carriers across the direct band gap of germanium (0.8 eV, indirect gap 0.66 eV), yielding a carrier density of $\sim 3 \times 10^{20}\,\mathrm{cm}^{-3}$ [Fig. 1(b)], which corresponds to an excitation of 0.6% of the germanium atoms. The resulting excited carrier distribution is then probed via transitions from Ge 3*d* ($J = 5/2$ and $3/2$, spin-orbit splitting 0.57 eV) core states to unoccupied states in the valence and conduction bands [17] by measuring the transient reflectivity defined as $\Delta R/R = [R_p(E,\tau) - R_0(E)]/R_0(E)$, where $R_0(E)$ and $R_p(E,\tau)$ are the intensity of reflected signal from the static (unpumped, 0), and excited sample (pumped, p), respectively.

The Ti:sapphire amplifier produces 1.7 mJ, 25 fs pulses at a 1 kHz repetition rate. The pulses are then compressed to sub 5-fs duration (corresponding to less than 2 optical cycles) and 800 μJ pulse energy using self-phase modulation in a neon-filled hollow core fiber and chirped mirror compressor (Ultrafast Innovations optics). Few-cycle compression is a prerequisite for generation of an XUV continuum (see Supplemental Material [51]), which greatly enhances signal to noise over the required large XUV bandwidth in the experiment. The usable compressed pulse bandwidth extends from 550–1000 nm, and the pulses are characterized using a dispersion scan [18] showing a pulse duration of < 5 fs (Supplemental Material [51]). The compressed output is split with a 60:40 beam splitter. Sixty percent of the energy (480 μJ) is used to generate the probe via HHG. High harmonics are produced by focusing into a Xe gas target, yielding continuous harmonic spectra from 25–40 eV (Supplemental Material [51]). Residual NIR from the generation process is removed with a 100-nm-thick Al filter. The XUV probe is then focused onto the sample

using a grazing incidence gold-coated toroidal mirror. The remaining 40% pump of the energy is time delayed using a retroreflector on a piezostage and recombined collinearly with the probe using an annular mirror. The NIR pump pulse is focused to 200 μm (FWHM) diameter onto the sample, and the XUV beam is focused to ~100 μm (FWHM) diameter.

Single-crystal germanium [100] wafers, undoped, were obtained from commercial sources. Any ambient oxide is not removed. The static (unpumped) dielectric function of the sample was measured by fitting reflectivity measured at six angles with synchrotron radiation, *s*-polarized, to the Fresnel equations [19]:

$$R_s = \left| \frac{n_1 \cos\theta_i - n_2 \sqrt{1 - \left(\frac{n_1}{n_2}\sin\theta_i\right)^2}}{n_1 \cos\theta_i + n_2 \sqrt{1 - \left(\frac{n_1}{n_2}\sin\theta_i\right)^2}} \right|^2, \quad (1)$$

where $n_2 = \sqrt{\epsilon}$ is the complex valued index of refraction of the wafer, θ_i is the angle of incidence measured from normal, and n_1 is the index of refraction of the vacuum. Since the pressure in the experimental chamber is $\sim 1 \times 10^{-7}$ Torr, we take n_1 to be 1. Static reflectivity measurements were performed at the Advanced Light source at Lawrence Berkeley National Laboratory.

III. RESULTS AND DISCUSSION

A. Transient reflectivity

The static reflectivity spectrum shown in Fig. 1(c) is characterized by a sharp decrease and subsequent increase of the reflectivity around the Ge $M_{4,5}$ edge (29.2, 29.8 eV), corresponding to transitions from the $3d_{5/2,3/2}$ core states into unoccupied states in the valence and conduction bands. The onset of the reflectivity increase around 30 eV mimics the evolution of the imaginary part of the refractive index, i.e., the absorbance of the material (Supplemental Material [51] Fig. 1).

The transient XUV reflectivity changes, $\Delta R/R$ as a function of pump-probe delay and reflected photon energy are shown in Fig. 1(d). The transient features observed can be broadly classified as follows: a decrease in reflectivity from 28–29 eV that persists for at least 10 ps (feature 1), an increase in reflectivity from 29–30 eV (feature 2) that decays within 3 ps, and a pair of features at 30.1 and 30.7 eV (feature 3) that gradually grow in on a many-picosecond timescale.

Ultimately, the transient features in Fig. 1(d) need to be linked to the pump-induced creation of holes in the valence band (below 29.2–29.8 eV), electrons in the conduction band (above 29.8–30.4 eV), and the subsequent relaxation processes [3]. Both features 1 and 2 lie below the formal onset of the conduction band (29.8 eV), requiring a detailed analysis (discussed below) to make this link and to spectroscopically assign features 1, 2, and 3. The analysis also considers the 3*d* spin-orbit splitting of the major features due to electrons and holes.

B. Decomposition of transient reflectivity into carriers and energy shift

The recorded transient reflectivity [Fig. 1(d)] results from changes in the real and imaginary parts of the dielectric function of germanium due to state-blocking by excitation of both electrons and holes and energy level shifts due to changes in core-hole screening and phonon dynamics. In order to disentangle and recover these separate effects from the XUV transient reflectivity data, we start with the premise that the changes to the dielectric function can be fit by a sum of a few complex oscillator terms. Thus a fit of the transient reflectivity data is made via Eq. (1) to an excited state transient dielectric function, $\varepsilon_{\rm exc}(\omega)$, of the following form:

$$\begin{aligned}
\varepsilon_{\rm exc}(\omega) &= \varepsilon_{\rm shift}(\omega) + \varepsilon_{\rm carrier}(\omega) \\
&= \varepsilon_{\rm shift}(\omega) + \varepsilon_{\rm holes}(\omega) + \varepsilon_{\rm electrons}(\omega), \\
\varepsilon_{\rm exc}(\omega) &= \varepsilon_0(\omega - {\rm E}_{\rm shift}) + \frac{\omega_{p,h}^2}{\omega_{0,h}^2 - \omega^2 + i\omega\Gamma_h} \\
&\quad - \frac{\omega_{p,e}^2}{\omega_{0,e}^2 - \omega^2 + i\omega\Gamma_e}, \quad (2)
\end{aligned}$$

where $\varepsilon_{\rm shift}(\omega)$ and $\varepsilon_{\rm carrier}(\omega)$ represent contributions to the dielectric function from global shifts and the carriers (electrons + holes), respectively. In Eq. (2), $\varepsilon_0(\omega)$ is the ground-state dielectric function (measured by multiangle reflection), and $\varepsilon_0(\omega - E_{\rm shift})$ describes the impact of global shifts to the excited state dielectric function, which physically corresponds to the energy shifts of the core-level or the unoccupied conduction band states. The two Lorentzian terms are Lorentz-Drude oscillators, one for the electron and one for the hole contributions to the excited state dielectric function. The Lorentz-Drude model is frequently used to model the dielectric function in the optical, UV, or XUV frequency ranges [20,21].

The two oscillators are described by the parameters $\omega_{p,h}$, $\omega_{p,e}$, $\omega_{0,h}$, $\omega_{0,e}$, Γ_h, and Γ_e, which include the amplitude, central frequency, and width of excited electron and hole induced changes to the dielectric function. At each time-delay point, the broadband transient reflectivity signal is fit to (2), giving a parameterization of the excited state dielectric function in terms of electron, hole, and global shift contributions, and allowing separation of the transient contribution from each term.

Previous work accounted for the spin-orbit splitting of the core hole by deconvolving the dynamics under the assumption that the $3d_{5/2}$ and $3d_{3/2}$ core states give rise to a statistical distribution of transient features, with ratios 3:2 [3,4]. In the presented model, this would be accounted for by splitting each oscillator into two components, spaced by the spin-orbit splitting (0.57 eV), with a set amplitude ratio of 3:2. Fitting using this model is unable to match the experimental data. This could be due to the broad nature and complex shape of the $M_{4,5}$ transition, especially in the dispersive part of the dielectric [17], and it will be shown below that the real part of the dielectric function dominates the reflected signal at the specific angle used here. There could also be a nonstatistical branching ratio from the two spin-orbit core-level states [22–24]. Both of these could result in the $M_{4,5}$ edge being experimentally better fit a single, broadened transition. Consequently, we use only two oscillators, one for the electrons, and one for the holes, to model changes to the dielectric function near the $M_{4,5}$ edge. As shown below, this simple model provides a very good description of the observed dynamics, further justifying the

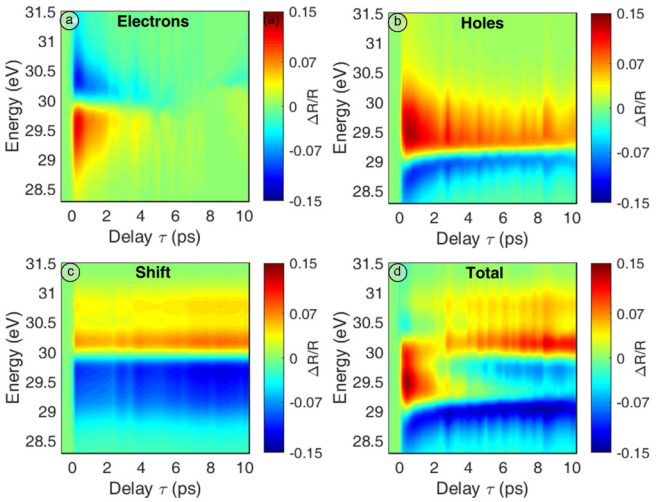

FIG. 2. Transient reflectivity modeling and decomposition. (a) Electron contribution to $\Delta R/R$ computed from dielectric function fit in Eq. (1). (b) Hole contribution to $\Delta R/R$ computed from dielectric function fit. (c) Shift contribution to $\Delta R/R$ computed from the dielectric function fit. (d) Total recovered $\Delta R/R$ computed from the dielectric function fit.

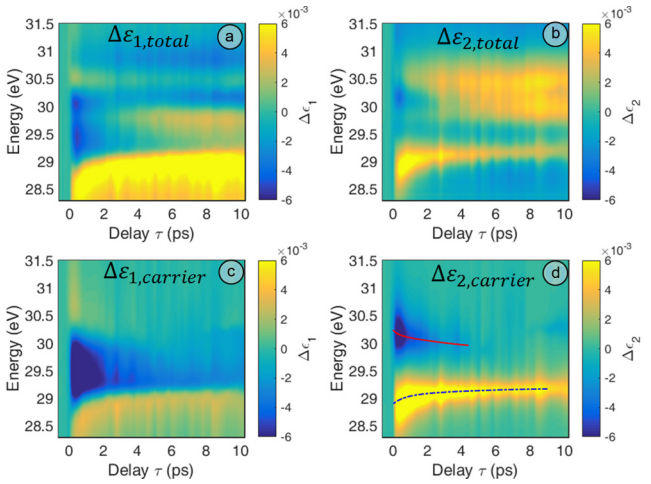

FIG. 3. Recovered time-resolved dielectric function. (a) Transient dispersive $\Delta\varepsilon_1$ retrieved from model. (b) Transient absorptive $\Delta\varepsilon_2$ retrieved from model. (c) Carrier contribution to $\Delta\varepsilon_1$ retrieved from model. (d) Carrier contribution to $\Delta\varepsilon_2$ retrieved from model, showing carrier center energies of electrons (red line), and holes (blue line), respectively.

simplying assumption of a single oscillator for each electrons and holes.

The extracted reflectivity contributions for the holes, electrons, and shifts [Figs. 2(a)–2(c)] allow assignment of the features in the experimental data. The total recovered transient reflectivity [Fig. 2(d)] closely tracks the experimental data [Fig. 1(d)] indicating that the model captures the dynamics present. The transient reflectivity contributions of both holes and electrons show a dispersive line profile at each time delay. This dispersion line has opposite signs for electrons and holes, and it changes sign at the center energy of the carriers, resulting from the fact that the electrons and holes have opposite effects on the available states for XUV transitions. Holes contribute a depletion from 28.3 to 29 eV and an increase from 29 to 31 eV, which narrows, but persists for the entire 10 ps duration of the measurement [Fig. 2(a)]. Electrons contribute an increase from 28.3 to 30 eV and a depletion from 30 to 31.5 eV, which decays within approximately 4 ps [Fig. 2(b)]. The global shift contributes a depletion below 29.9 eV and an increase above 29.9 eV, which gradually increases on a longer timescale.

Interestingly, both the electron and hole $\Delta R/R$ contributions in Figs. 2(a) and 2(b) show broadband changes spanning from a 3.2 eV range from 28.3 to 31.5 eV, including changes within the band gap region ~29–30 eV. This is because $\Delta R/R$ is sensitive to both ε_1 in addition to ε_2. Previous work has observed changes to the dispersive ε_1 in the gap region of semiconductors following interband excitation [25]. Accordingly, we attribute $\Delta R/R$ in the gap region to pump-induced changes in ε_1.

C. Assignment of time resolved dielectric function

The transient dielectric function, $\Delta\varepsilon(\omega) = \varepsilon_{\text{exc}}(\omega) - \varepsilon_0(\omega)$, was recovered from the fit of the experimental data to Eq. (2) and is shown in Figs. 3(a) and 3(b). The real part, $\Delta\varepsilon_1$, shows a transient depletion from 29–30 eV right at the $M_{4,5}$ edge, persisting for 4 ps, and an increase below 29 eV, which persists out to 10 ps. The imaginary part, $\Delta\varepsilon_2$, shows a persistent increase from 28.5 to 29.3 eV (just below the $M_{4,5}$ edge), and a transient depletion from 29.9 to 31 eV (just above the $M_{4,5}$ edge), which is replaced by an increase growing in within around 4 ps. Both $\Delta\varepsilon_1$ and $\Delta\varepsilon_2$ shift toward the $M_{4,5}$ edge (29.6 eV) on a multipicosecond timescale.

To aid in assignment of the features in the transient dielectric function, the carrier contributions to the transient dielectric function ($\Delta\varepsilon_{\text{carrier}} = \Delta\varepsilon_{\text{electrons}} + \Delta\varepsilon_{\text{holes}}$) are shown in Figs. 3(c) and 3(d). Comparing the carrier contributions to the total contributions reveals that most of the features of $\Delta\varepsilon_{1,\text{total}}$ and $\Delta\varepsilon_{2,\text{total}}$ near the $M_{4,5}$ edge come from the carrier contributions to the transient dielectric function. Indeed, the depletion in $\Delta\varepsilon_{1,\text{total}}$ below 29 eV and transient increase from 29–30 eV are well captured by the carrier contribution, $\Delta\varepsilon_{1,\text{carrier}}$ Similarly, the increase below 29.6 eV and depletion above 29.8 eV present in $\Delta\varepsilon_{2,\text{total}}$ is almost entirely captured by features in the carrier contribution, $\Delta\varepsilon_{2,\text{carrier}}$.

Near the Ge $M_{4,5}$ edge, the XUV dielectric function is dominated by direct, interband transitions from the $3d$ core levels, to unoccupied states in the valence and conduction bands [26,27]. Accordingly, the imaginary part of the linear dielectric function can be written as [28]

$$\varepsilon_2(\omega) = 8\left(\frac{\pi e}{m\omega}\right)^2 \sum_f \left|P_{ft}\right|^2 J_{ft}(\omega), \tag{3}$$

where e is the electron charge, m is the electron mass, p_{fi}, is the transition dipole matrix element between the initial and final states, J_{fi} is the joint density of states, f runs over all unoccupied states, and i refers to the $3d$ core states. Inspecting (3) reveals that carriers created by the pump can modify the XUV dielectric function either through state blocking (represented as a change in the joint density of states) or though renormalization of the $3d$ core hole potential manifesting as a change in the transition matrix element and the joint density

of states). Consequently, the amplitude $\Delta\varepsilon_2$ can be directly related to modifications of the density of states (i.e., state blocking by an excited carrier distribution), weighted by the transition dipole moment.

Because $\Delta\varepsilon_2$ is directly related to the change in XUV absorption of the material [29], we can interpret the transient features in $\Delta\varepsilon_{2,\text{carrier}}$ near the band edge as arising from state blocking of the $M_{4,5}$ transition by photoexcited carriers. The NIR pump promotes electrons from the valence band (VB) to the conduction band (CB), creating holes in the VB. The electrons in the CB reduce the available density of states for transitions from the $3d$ core levels, resulting in the transient depletion of $\Delta\varepsilon_2$ from 30–31 eV [Fig. 3(d)]. Similarly, holes in the VB increase the available density of states for core-level transitions, resulting in a positive $\Delta\varepsilon_2$ below the band edge. The assignment of $\Delta\varepsilon_2$ features to state blocking is supported by recent XUV transient absorption in germanium in which similar state blocking contributions were observed near the $M_{4,5}$ edge [3].

D. Enhanced sensitivity to ε_1

To better understand the relationship between the measured transient reflectivity in Fig. 1(d) and the recovered transient dielectric function, we computed the transient reflectivity contributions from the measured real and imaginary parts of the transient dielectric function [Figs. 4(a) and 4(b)]. For example, the imaginary contribution [Fig. 4(a)] was computed as follows:

$$\frac{\Delta R}{R}(\Delta\varepsilon_2) = \frac{\Delta R}{R}(\text{Re}(\varepsilon_0) + \text{i}\,\text{Im}(\varepsilon_{\text{exc}})), \tag{4}$$

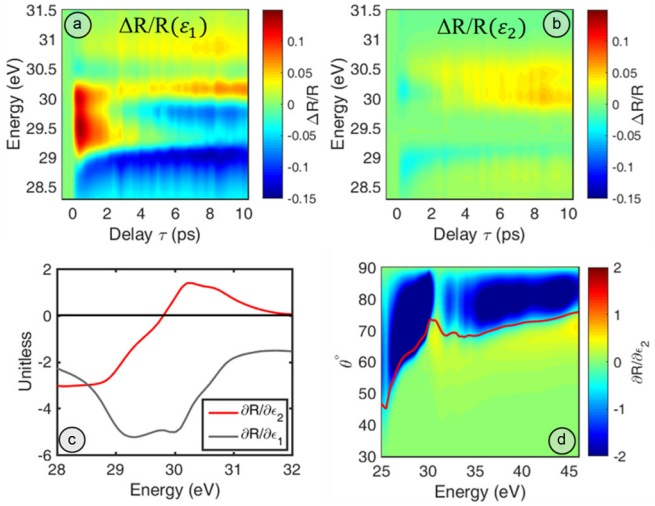

FIG. 4. Sensitivity of transient reflectivity to ε_1: (a) $\Delta R/R$ computed with static ε_1 and transient ε_2 retrieved with model. (b) $\Delta R/R$ computed with static ε_1 and transient ε_2. (c) Red, $\partial R/\partial\varepsilon_2$ at experimental angle of incidence (66), computed from static dielectric function, showing zero at 29.8 eV. Grey, $\partial R/\partial\varepsilon_1$ at experimental angle of incidence (66), computed from static dielectric function, showing no zero. (d) Heatmap: $\partial R/\partial\varepsilon_2$ as a function of angle of angle of incidence, computed from static dielectric function. Red line: critical angle for XUV computed from static dielectric function, clearly tracking the zero of $\partial R/\partial\varepsilon_2$.

where ε_0 and ε_{exc} are the (static) ground and excited state dielectric functions from Eq. (2). Despite the fact that dispersive $\Delta\varepsilon_1$ and absorptive $\Delta\varepsilon_2$ are both of similar magnitudes, the majority ($74 \pm 10\%$) of the $\Delta R/R$ signal observed over the range of 28.3-31.5 eV can be attributed to the $\Delta\varepsilon_1$ (real) contribution [Fig. 4(a)]. The $\Delta\varepsilon_2$ (imaginary) contribution [Fig. 4(b)] by contrast is smaller, contributing only $26 \pm 10\%$ of the reflectivity changes from 28.3–31.5 eV. The insensitivity of the measured transient reflectivity signal to $\Delta\varepsilon_2$ near the $M_{4,5}$ edge can be explained by examining $\partial R/\partial\varepsilon_1$ and $\partial R/\partial\varepsilon_2$, which are shown in Fig. 4(c). For small $\Delta\varepsilon$, the magnitude of the computed derivatives in Fig. 4(c) provides an estimate of the sensitivity of the transient reflectivity to the real and imaginary parts of the dielectric function. Over the range of 28.3 to 31.5 eV, $\partial R/\partial\varepsilon_1$ contributes 72% of the total derivative, indicating that relative sensitivity of $\Delta R/R$ to $\Delta\varepsilon_1$ can be mainly explained by the static ground-state dielectric function. Interestingly, due to the zero crossing at 29.8 eV, from 29.7 to 29.9 eV $\Delta\varepsilon_2$ contributes less than 5% to the total derivative, indicating a substantial lack of sensitivity to $\Delta\varepsilon_2$ in this region.

More intuitively, the lack of sensitivity to $\Delta\varepsilon_2$ at 29.8 eV can be explained by the fact that at this energy, the angle of incidence is near the critical angle for germanium. This is illustrated in Fig. 4(d), which shows $\partial R/\partial\varepsilon_2$ computed as a function of the angle of incidence (heat map), overlaid with the critical angle (red line), computed as $\sqrt{2(1-n)}$, where n is the real part of the ground state refractive index (recovered from the multi angle fit described in the SI). Interestingly, the critical angle closely tracks the zero of $\partial R/\partial\varepsilon_2$, indicating that $\partial R/\partial\varepsilon_2$ can be selectively tuned to greater or lower values by changing the angle of incidence nearer or further from the critical angle. Consequently, near-critical-angle transient reflectivity allows for selective sensitivity to ε_1 in many systems. In light of recent work demonstrating that the real part of the index of refraction shows enhanced surface sensitivity [15], the prospect of selective probing through the dispersive ε_1 provides a promising approach to achieve enhanced surface sensitivity with XUV transient reflectivity.

E. Carrier and phonon thermalization kinetics

The dielectric function extracted in Figs. 3(a) and 3(b) allows determination of carrier dynamics initiated by the NIR pump. The electron and hole positions, extracted by the fit to Eq. (1), are shown in Fig. 5(a), along with biexponential fits. Both features show a rapid shift toward the band edge ($\tau_1 = 600 \pm 300$ fs for holes, $\tau_1 = 400 \pm 300$ fs for electrons) followed by slower shifts toward the respective band edges ($\tau_2 = 4.8 \pm 0.7$ ps for holes, $\tau_2 = 5.5 \pm 1.2$ ps for electrons), which are similar within experimental error.

The timescale of the initial rapid decay of the carrier features toward the band edge is consistent with thermalization of the hot carrier distributions by carrier-carrier and carrier-phonon scattering following excitation with the pump. Because these dynamics have been studied in detail recently in the XUV [3], and thoroughly in the past [30–32], we only provide a brief discussion here. For holes, thermalization is dominated by intravalley scattering within the heavy hole band, which should occur on a timescale of approximately 600 fs [30]. Consequently, we assign the 600-fs hole relaxation time to

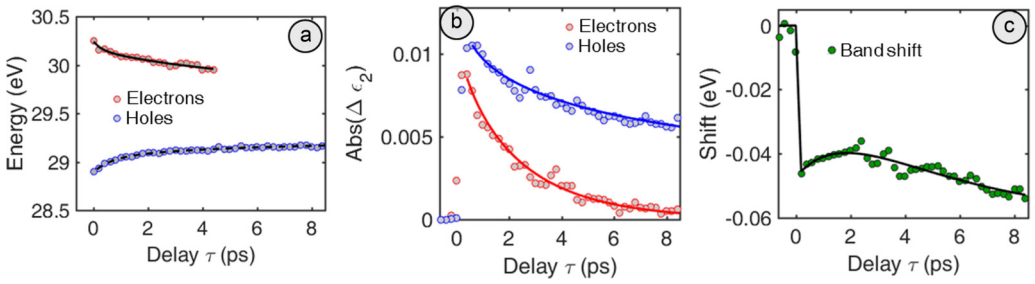

FIG. 5. Kinetics extracted from dielectric fit. (a) Electron (red) and hole (blue) positions (central energies) obtained from Eq. (3) with biexponential fits. The electron position stops at 4 ps due to depletion of electron signal. (b) $\Delta\varepsilon_2$ obtained for electrons (red) and holes (blue) with fits from model (see text). (c) Redshift extracted from modeled dielectric function, along with biexponential fit.

intravalley scattering within the HH band. For electrons, the rapid decay toward the band edge is dominated by intervalley scattering from the Γ and L valleys to the X valley, due to its high density of states [30,31]. Accordingly, we attribute the 400 fs timescale to electron thermalization, mediated by Γ-X and L-X intervalley scattering. Note the large error bars on this number specified above.

The timescale of the slower shifts toward the respective band edges ($\tau_2 = 4.8$ ps for holes, $\tau_2 = 5.5$ ps for electrons) is too slow to be attributed to thermalization of the excited electronic distribution [as seen in Fig. 5(a)], which has been observed to occur in <1 ps [33]. Instead, we propose that the slower carrier shifts track the renormalization of the band gap by acoustic phonons created by electron-phonon and phonon-phonon scattering [34]. Initially, the pump produces an excited electron distribution with nearly 8000 K of excess kinetic energy. These carriers should then thermalize via carrier-phonon scattering (∼10s–100s of fs), resulting in a buildup of optical phonons [35]. Optical phonons then decay via anharmonic decay into two lower-energy acoustic phonons [36]. The resulting acoustic phonons then modify the band gap via either electron-phonon coupling, or thermally induced lattice expansion [37–39]. The observed timescales are inconsistent with previous work which observed thermally induced lattice expansion in germanium on a much longer time scale (75 ps) [40]. Accordingly, we attribute the band gap shrinkage to the renormalization by acoustic phonons, which results in the apparent movement of the carrier energies in Fig. 4(a) toward the band gap. In this case, we can then identify the time constants of 4.8 and 5.5 ps (similar within error) as decay times for anharmonic decay of an optical phonon into two acoustic phonons. Our measured decay times match well with LO lifetimes of 4 ps, previously measured in Ge [41]. Accordingly, we attribute the 4.8- and 5.5-ps timescales to decay of the LO phonon population, which tracks the thermally induced bang gap shift.

Lineouts along the maximum of the electron and hole features from 3d are incorporated into Fig. 5(b), showing the decay of the electron and hole contributions to the absorptive $\Delta\varepsilon_2$. Both contributions decay rapidly, although the decay cannot be well fit with a single exponential. By definition, the carrier contribution to $\Delta\varepsilon_2$ is directly proportional to excited carrier density, weighted by the XUV transition dipole element [Eq. (3)], hence decay of the transient dielectric function modification reports on two processes: depletion of the excited carrier distribution and intervalley scattering of the carrier distribution between regions of different XUV oscillator strengths.

The fact that the electron- and hole-induced dielectric changes [Fig. 5(b)] show substantial decay within 10 ps means that surface recombination cannot explain the kinetics observed, as carrier recombination is observed to occur on the μs timescale [42]. To further understand the origin of the electron and hole kinetics, we modeled the spatial evolution of the excited carrier distribution after excitation (Supplemental Material [51]), including Auger recombination, and a temperature dependent diffusion constant [32,43–46]. Because the pump is much larger than the probe (Supplemental Material [51]), diffusion parallel to the surface of the wafer is neglected, and only diffusion normal to the surface is considered [32]. By assuming that $\Delta\varepsilon_2$ is proportional to the surface carrier density, our simulations [blue solid line in Fig. 5(b)] recreate the hole kinetic trace (blue circles) using an initial carrier density of $3 \times 10^{20}\,\mathrm{cm}^{-3}$. Based on the agreement with simulations, we attribute the depletion of the hole signal to diffusion of holes out of the probe interaction region, in conjunction with Auger recombination, in which an electron and hole recombine and transfer excess energy to another electron or hole. These results agree with previous work in germanium, in which carrier diffusion was shown to play a substantial role in hole bleaching on a 6-ps timescale [32].

By contrast, the electron contribution to $\Delta\varepsilon_2$ decays more rapidly and is almost entirely gone by 3 ps. This depletion cannot be explained by a combination of diffusion and Auger recombination, as both of these processes should lead to a persistent signal for over 10 ps (Supplemental Material [51]). Previous studies have shown that initial excitation in germanium results in rapid transfer of population from the Γ-X valleys, via deformation potential interaction (∼200 fs), followed by slow transfer of population of electrons from X-L within ∼3 ps [30,32]. Because the L valley is mainly Ge 4s character, while the X valley is mainly Ge 4p character, XUV transitions from the 3d core state to the L valley are forbidden by angular momentum selection rules, while transitions to the X valley are allowed [3]. Thus electron scattering from the X to the L valleys should result in a depletion of electron signal. Accordingly, we model the depletion of the electron contribution to $\Delta\varepsilon_2$ by considering Auger recombination, diffusion, and a single exponential decay representing X-L intervalley scattering Fig. 5(b), red line. This allows extraction of an X-L population transfer time constant of 3.2 ± 0.2 ps, which is in good agreement with previous results [30].

TABLE I. Recovered time constants and assigned processes

Time constant	Error	Process	Source
600 fs	300 fs	Hole relaxation	Carrier center
400 fs	300 fs	Electron relaxation	Carrier center
1.8 ps	0.4 ps	Diffusion/Recombination	Band shift decay
3.2 ps	0.2 ps	*X-L* Electron scattering	Electron signal decay
4.0 ps	1.0 ps	LO Phonon lifetime	Band shift growth
4.8 ps	0.7 ps	LO Phonon lifetime	Carrier center
5.5 ps	1.2 ps	LO Phonon lifetime	Carrier center

The transient band shift extracted from Eq. (2) is shown in Fig. 5(c). It is fit with a combined step function and biexponential decay and rise of the redshift (note negative numbers on the graph) with time constants of 1.8 ± 0.4 and 4.0 ± 1.0 ps. The timescale of the rapid initial redshift is too rapid to distinguish in the longer time experiments emphasized here, and it is accordingly attributed to a carrier induced dynamic redshift of the conduction band due to screening by carriers [47]. The observation is additionally supported by a similar carrier induced dynamic redshift in XUV transient absorption in germanium [3]. Previous work has shown that the redshift of the conduction band should scale as the cube root of the excited carrier density [48]. Accordingly, the 1.8-ps decay of the redshift is thus attributed to a depletion of carriers, via Auger recombination and diffusion. Because the rate of Auger recombination goes as n^3, (where n is the carrier density) initially, recombination is relatively faster, and it slows down as recombination occurs. Accordingly, the recovered 1.8-ps timescale retrieved for the band shift should not result in complete depletion of the carriers within 1.8 ps, and this is consistent with the observation of excited carriers out to 10 ps. Finally, the 4 ± 1.0 ps growth of the redshift is attributed to band gap renormalization by the population of acoustic phonon modes, which matches previously measured optical phonon lifetimes [49]. Within error, the agreement of the 4-ps redshift with the 4.8- and 5.5-ps timescales shown in Fig. 5(a) provides further support to the assignment of these processes to phonon decay, since all three timescales should ultimately report on the same process. The recovered time constants, their associated errors, and the assigned processes are summarized below in Table I. Although the LO phonon lifetimes derived from the band shift, electron carrier center, and hole carrier center differ slightly, the time constants retrieved are consistent within error. The impact of acoustic phonon induced gap shrinkage is expected to differ for different bands [43,50]. Because the 4-ps timescale obtained from the band shift [Fig. 5(c)] is obtained from a global shift of the entire static spectrum, it should be the most reliable, since it should average out differences in the valley specific band shifts. Accordingly, we take the 4-ps timescale to be the LO phonon lifetime, in good agreement with previous work.

IV. CONCLUSION

XUV transient reflectivity at the Ge $M_{4,5}$ edge was developed, and a framework for interpreting the XUV spectral changes in terms of electron, hole, and phonon contributions spectral contributions was reported. This framework allows simultaneous, independent measurement of electron, hole, and phonon thermalization processes as well as recovery of the time dependent dielectric function following photoexcitation. Further analysis reveals that under our experimental conditions near the critical angle, the XUV TR is dominated by changes to the real part of the dielectric function. Retrieval of the real ε_1 and imaginary ε_2 allows tracking of carrier centers of energy and relative populations, allowing independent thermalization rates to be simultaneously measured. Hot electron relaxation via Γ-X and L-X intervalley scattering are observed within 400 ± 300 fs, hot hole relaxation via intravalley scattering within the HH band are observed within 600 ± 300 fs, in agreement with previous work [30]. Additionally, electron X-L intervalley scattering was observed within 3.2 ± 0.2 ps. Band gap renormalization by electron-phonon coupling via acoustic phonons, previously unresolvable in XUV absorption measurements, was observed within 4–5 ps, in good agreement with previously measured optical phonon lifetimes [41]. The agreement of the observed relaxation kinetics with those previously measured using optical methods highlights the fact that XUV transient reflectivity can be used quantify the carrier dynamics and band gap shifts in semiconductors, and the method can overcome the thin sample issues associated with XUV Transient absorption. The framework put forth in this work allows for rigorous interpretation of XUV Transient Reflectivity spectral components, and opens the door for attosecond investigation of ultrafast process in materials that are inaccessible by absorption methods.

ACKNOWLEDGMENTS

C.J.K. acknowledges support by the Defense Advanced Research Projects Agency PULSE program through grant W31P4Q-13-1-0017. P.M.K. acknowledges support from the Swiss National Science Foundation (Grant Nos. P2EZP2_165252 and P300P2_174293). M.Z. acknowledges support by the Army Research Office (ARO) (WN911NF-14-1-0383). S.K.C. acknowledges a postdoctoral fellowship through the Office of Energy Efficiency and Renewable Energy of the Department of Energy M.Z. acknowledges support from the Humboldt Foundation. H.-T.C. acknowledges support by the Air Force Office of Scientific Research (AFOSR) (FA9550-15-1-0037). The initial instrument development and experimental work was supported by the Office of Assistant Secretary of Defense for Research and Engineering through a National Security Science and Engineering Faculty Fellowship (NSSEFF) and W.M. Keck Foundation.

C.J.K. and P.M.K. each contributed equally to this work.

[1] J. Shah, *Ultrafast Spectroscopy of Semiconductors and Semiconductor Nanostructures* (Springer Science & Business Media, 2013).

[2] D. König, K. Casalenuovo, Y. Takeda, G. Conibeer, J. F. Guillemoles, R. Patterson, L. M. Huang, and M. A. Green, Phys. E Low-Dimensional Syst. Nanostructures **42**, 2862 (2010).

[3] M. Zürch, H.-T. Chang, L. J. Borja, P. M. Kraus, S. K. Cushing, A. Gandman, C. J. Kaplan, M. H. Oh, J. S. Prell, D. Prendergast, C. D. Pemmaraju, D. M. Neumark, and S. R. Leone, Nat. Commun. **8**, 15734 (2017).

[4] M. Zürch, H.-T. Chang, P. M. Kraus, S. K. Cushing, L. J. Borja, A. Gandman, C. J. Kaplan, M. H. Oh, J. S. Prell, D. Prendergast, C. D. Pemmaraju, D. M. Neumark, and S. R. Leone, Struct. Dyn. **4**, 044029 (2017).

[5] C.-M. Jiang, L. R. Baker, J. M. Lucas, J. Vura-Weis, A. P. Alivisatos, and S. R. Leone, J. Phys. Chem. C **118**, 22774 (2014).

[6] M. F. Jager, C. Ott, P. M. Kraus, C. J. Kaplan, W. Pouse, R. E. Marvel, R. F. Haglund, D. M. Neumark, and S. R. Leone, Proc. Natl. Acad. Sci. USA **114**, 9558 (2017).

[7] M. Schultze, K. Ramasesha, C. D. Pemmaraju, S. A. Sato, D. Whitmore, A. Gandman, J. S. Prell, L. J. Borja, D. Prendergast, K. Yabana, D. M. Neumark, and S. R. Leone, Science **346**, 1348 (2014).

[8] S. Mathias, C. La-O-Vorakiat, P. Grychtol, P. Granitzka, E. Turgut, J. M. Shaw, R. Adam, H. T. Nembach, M. E. Siemens, S. Eich, C. M. Schneider, T. J. Silva, M. Aeschlimann, M. M. Murnane, and H. C. Kapteyn, Proc. Natl. Acad. Sci. USA **109**, 4792 (2012).

[9] D. Zusin, P. M. Tengdin, M. Gopalakrishnan, C. Gentry, A. Blonsky, M. Gerrity, D. Legut, J. M. Shaw, H. T. Nembach, T. J. Silva, P. M. Oppeneer, H. C. Kapteyn, and M. M. Murnane, Phys. Rev. B **97**, 024433 (2018).

[10] E. Turgut, D. Zusin, D. Legut, K. Carva, R. Knut, J. M. Shaw, C. Chen, Z. Tao, H. T. Nembach, T. J. Silva, S. Mathias, M. Aeschlimann, P. M. Oppeneer, H. C. Kapteyn, M. M. Murnane, and P. Grychtol, Phys. Rev. B **94**, 220408 (2016).

[11] S. Mathias, C. La-o-vorakiat, J. M. Shaw, E. Turgut, P. Grychtol, R. Adam, D. Rudolf, H. T. Nembach, T. J. Silva, M. Aeschlimann, C. M. Schneider, H. C. Kapteyn, and M. M. Murnane, J. Electron Spectros. Relat. Phenomena **189**, 164 (2013).

[12] E. Turgut, C. La-o-vorakiat, J. M. Shaw, P. Grychtol, H. T. Nembach, D. Rudolf, R. Adam, M. Aeschlimann, C. M. Schneider, T. J. Silva, M. M. Murnane, H. C. Kapteyn, and S. Mathias, Phys. Rev. Lett. **110**, 197201 (2013).

[13] R. Berlasso, C. Dallera, F. Borgatti, C. Vozzi, G. Sansone, S. Stagira, M. Nisoli, G. Ghiringhelli, P. Villoresi, L. Poletto, M. Pascolini, S. Nannarone, S. De Silvestri, and L. Braicovich, Phys. Rev. B **73**, 115101 (2006).

[14] A. Cirri, J. Husek, S. Biswas, and L. R. Baker, J. Phys. Chem. C **121**, 15861 (2017).

[15] J. Husek, A. Cirri, S. Biswas, and L. R. Baker, Chem. Sci. 8170 (2017).

[16] F. Krausz and M. Ivanov, Rev. Mod. Phys. **81**, 163 (2009).

[17] B. L. Henke, E. M. Gullikson, and J. C. Davis, Nucl. Data Table **54**, 181 (1993).

[18] F. Silva, M. Miranda, B. Alonso, J. Rauschenberger, V. Pervak, and H. Crespo, Opt. Express **22**, 10181 (2014).

[19] D. J. Griffiths and C. Inglefield, *Introduction to Electrodynamics*, 4th ed. (Cambridge University Press, 2017).

[20] C. Kittel, *Introduction to Solid State Physics* (Wiley, 2005).

[21] D. Attwood, *Soft X-Rays and Extreme Ultraviolet Radiation: Principles and Applications*, 1st ed. (Cambridge University Press, New York, NY, USA, 2007).

[22] W. L. O'Brien, J. Jia, Q.-Y. Dong, T. A. Callcott, J.-E. Rubensson, D. L. Mueller, and D. L. Ederer, Phys. Rev. B **44**, 1013 (1991).

[23] B. T. Thole and G. van der Laan, Phys. Rev. B **38**, 3158 (1988).

[24] A. Scherz, *Spin-Dependent X-Ray Absorption Spectroscopy of 3d Transition Metals: Systematics and Applications* (Free University of Berlin, 2003).

[25] T. Shih, M. T. Winkler, T. Voss, and E. Mazur, Appl. Phys. A **96**, 363 (2009).

[26] B. Feurbacher, M. Skibowski, R. P. Godwin, and T. Sasaki, **58**, 1434 (1969).

[27] M. Taniguchi, S. Suga, S. Shin, K. Inoue, M. Seki, and H. Kanzaki, Solid State Commun. **44**, 85 (1982).

[28] P. Y. Yu and M. Cardona, *Fundamentals of Semiconductors* (Springer-Verlag, Berlin Heidelberg, 2010).

[29] A. E. Siegman, *Lasers* (University Science Books, 1986).

[30] D. W. Bailey and C. J. Stanton, J. Appl. Phys. **77**, 2107 (1995).

[31] G. Mak and H. M. van Driel, Phys. Rev. B **49**, 16817 (1994).

[32] S. Zollner, K. D. Myers, K. G. Jensen, J. M. Dolan, D. W. Bailey, and C. J. Stanton, Solid State Commun. **104**, 51 (1997).

[33] X. Q. Zhou, H. M. van Driel, and G. Mak, Phys. Rev. B **50**, 5226 (1994).

[34] L. Viña, S. Logothetidis, and M. Cardona, Phys. Rev. B **30**, 1979 (1984).

[35] A. Othonos, J. Appl. Phys. **83**, 1789 (1998).

[36] A. Debernardi, S. Baroni, and E. Molinari, Phys. Rev. Lett. **75**, 1819 (1995).

[37] P. B. Allen and M. Cardona, Phys. Rev. B **23**, 1495 (1981).

[38] P. Lautenschlager, P. B. Allen, and M. Cardona, Phys. Rev. B **31**, 2163 (1985).

[39] P. B. Allen and M. Cardona, Phys. Rev. B **27**, 4760 (1983).

[40] A. Cavalleri, C. W. Siders, F. L. H. Brown, D. M. Leitner, C. Tóth, J. A. Squier, C. P. J. Barty, K. R. Wilson, K. Sokolowski-Tinten, M. Horn von Hoegen, D. von der Linde, and M. Kammler, Phys. Rev. Lett. **85**, 586 (2000).

[41] A. Othonos, H. M. van Driel, J. F. Young, and P. J. Kelly, Phys. Rev. B **43**, 6682 (1991).

[42] E. Gaubas and J. Vanhellemont, J. Electrochem. Soc. **154**, H231 (2007).

[43] S. K. Cushing, M. Zürch, P. M. Kraus, L. M. Carneiro, A. Lee, H.-T. Chang, C. J. Kaplan, and S. R. Leone, arXiv:1705.04393.

[44] T. Shin, S. W. Teitelbaum, J. Wolfson, M. Kandyla, and K. A. Nelson, J. Chem. Phys. **143**, 194705 (2015).

[45] J. F. Young and H. M. van Driel, Phys. Rev. B **26**, 2147 (1982).

[46] C. A. and E. of the L. V. III/17A-22A-41A1b, in *Gr. IV Elem. IV-IV III-V Compd. Part B - Electron. Transp. Opt. Other Prop.* (Springer-Verlag, Berlin/Heidelberg, n.d.), pp. 1–7.

[47] B. R. Bennett, R. A. Soref, and J. A. Del Alamo, IEEE J. Quantum Electron. **26**, 113 (1990).

[48] P. A. Wolff, Phys. Rev. **126**, 405 (1962).
[49] M. L. Ledgerwood and H. M. van Driel, Phys. Rev. B **54**, 4926 (1996).
[50] P. Ruello and V. E. Gusev, Ultrasonics **56**, 21 (2015).
[51] See Supplemental Material at http://link.aps.org/supplemental/10.1103/PhysRevB.97.205202 for a description of pulse characterization, static dielectric functions, and details of diffusion modeling mentioned in text.